© 2022. Published by The Company of Biologists Ltd | Development (2022) 149, dev200527. doi:10.1242/dev.200527

STEM CELLS AND REGENERATION

RESEARCH ARTICLE

Hbxip is essential for murine embryogenesis and regulates embryonic stem cell differentiation through activating mTORC1

Yan Qin*, Peiling Ni*, Qingye Zhang, Xiao Wang, Xiaoling Du, Zixi Yin, Lingling Wang, Lihong Ye‡ and Lingyi Chen‡

ABSTRACT

HBXIP, also named LAMTOR5, has been well characterized as a transcriptional co-activator in various cancers. However, the role of Hbxip in normal development remains unexplored. Here, we demonstrated that homozygous knockout of *Hbxip* leads to embryonic lethality, with retarded growth around E7.5, and that depletion of Hbxip compromises the self-renewal of embryonic stem cells (ESCs), with reduced expression of pluripotency genes, reduced cell proliferation and decreased colony-forming capacity. In addition, both *Hbxip*$^{-/-}$ ESCs and E7.5 embryos displayed defects in ectodermal and mesodermal differentiation. Mechanistically, Hbxip interacts with other components of the Ragulator complex, which is required for mTORC1 activation by amino acids. Importantly, ESCs depleted of Ragulator subunits, Lamtor3 or Lamtor4, displayed differentiation defects similar to those of *Hbxip*$^{-/-}$ ESCs. Moreover, *Hbxip*$^{-/-}$, *p14*$^{-/-}$ and *p18*$^{-/-}$ mice, lacking subunits of the Ragulator complex, also shared similar phenotypes, embryonic lethality and retarded growth around E7-E8. Thus, we conclude that Hbxip plays a pivotal role in the development and differentiation of the epiblast, as well as the self-renewal and differentiation of ESCs, through activating mTORC1 signaling.

KEY WORDS: Hbxip, Lamtor5, Embryogenesis, Embryonic stem cells, MTORC1

INTRODUCTION

Hepatitis B X-interacting protein (HBXIP, also known as LAMTOR5), was first identified as a binding factor to hepatitis B virus X protein (Melegari et al., 1998). In addition to its role in inhibiting the replication of hepatitis B virus, HBXIP has been extensively studied in various cancers. It has been shown that HBXIP promotes the proliferation, migration and tumorigenesis of breast, ovarian, liver, non-small-cell lung, bladder urothelial and esophageal squamous cell cancer (Hu et al., 2011; Liu et al., 2012, 2014; Xu et al., 2014; Zhang et al., 2014; Li and Liu, 2016; Shi et al., 2016; Wang et al., 2017b; Zhou et al., 2019b; Wu et al., 2020). Overexpression of HBXIP is associated with poor prognosis in breast, ovarian, liver, non-small-cell lung cancer and pancreatic ductal adenocarcinomas (Wang et al., 2017b,c; Li et al., 2017; Zhou et al., 2019a; Cheng et al., 2014). HBXIP also contributes to cisplatin and tamoxifen resistance in ovarian and breast cancers, respectively (Zou et al., 2017; Liu et al., 2018). However, the role of HBXIP in normal development remains poorly understood. Only a recent work reported that, owing to the pivotal role of Hbxip in activating the transcription of insulin by elevating the level of Pdx-1/Neurod1 complex, pancreatic β-cell-specific *Hbxip* knockout (KO) mice display higher fasting blood glucose levels and impaired glucose tolerance (Li et al., 2018).

The extensive studies of HBXIP in cancers have revealed its function as a transcriptional cofactor. HBXIP, cooperating with various transcription factors, such as c-MYB, SP1, cAMP response element-binding protein (CREB), TATA-binding protein (TBP) and E2F1, activates the expression of its downstream target genes, including *YAP*, *FGF8*, *LIN28B*, *SKP2*, *PDGFB*, *S100A4* and *LMO4*, consequently promoting the proliferation and migration of cancer cells (Liu et al., 2012, 2014, 2013; Xu et al., 2014, 2013; Yue et al., 2013; Zhang et al., 2013; Wang et al., 2017a). In addition, HBXIP may interact with proteins other than transcription factors to fulfill its biological functions. HBXIP interacts with survivin to suppress caspase activation and hence apoptosis (Marusawa et al., 2003). HBXIP also associates with microtubules and centrosomes in dividing cells, and is required for the proper formation of centrosomes and spindles in HeLa cells (Wen et al., 2008; Fujii et al., 2006). Moreover, HBXIP, together with p18 (LAMTOR1), p14 (LAMTOR2), MP1 (LAMTOR3) and C7ORF59 (LAMTOR4), form a pentameric Ragulator complex, which is required for mTORC1 activation by amino acids (Bar-Peled et al., 2012). Yet, whether HBXIP regulates normal development or carcinogenesis through the mTORC1 pathway remains unexplored.

In this study, we demonstrated that KO of *Hbxip* is embryonic lethal, and retarded development of *Hbxip*$^{-/-}$ embryos became obvious around E7.5. Using *Hbxip* KO embryonic stem cells (ESCs) as an *in vitro* model, we found that *Hbxip* is crucial for the differentiation of ESCs, particularly for ectodermal and mesodermal differentiation. Consistently, the epiblast of E8.5 *Hbxip*$^{-/-}$ embryos remained undifferentiated. The differentiation defects were shared by ESCs lacking subunits of the Ragulator complex, including Hbxip, Lamtor3 and Lamtor4. Thus, we conclude that Hbxip regulates embryo development and ESC differentiation through activating mTORC1 signaling.

RESULTS

Embryonic lethality in *Hbxip* null embryos

To study the function of Hbxip in normal development, we knocked out *Hbxip* in previously generated *Hbxip* floxed mice (Fig. 1A,B) (Li et al., 2018). Heterozygous *Hbxip* KO (*Hbxip*$^{+/-}$) mice were

Institute of Translational Medicine, Tianjin Union Medical Center, State Key Laboratory of Medicinal Chemical Biology, Tianjin Key Laboratory of Protein Sciences, Frontiers Science Center for Cell Responses, National Demonstration Center for Experimental Biology Education and College of Life Sciences, Nankai University, Tianjin 300071, China.
*These authors contributed equally to this work

‡Authors for correspondence (lingyichen@nankai.edu.cn; yelihong@nankai.edu.cn)

P.N., 0000-0002-4951-7356; X.W., 0000-0003-4368-7570; X.D., 0000-0001-7857-1688; Z.Y., 0000-0002-2044-5838; L.Y., 0000-0002-0089-7503; L.C., 0000-0002-3695-3407

Handling Editor: James Briscoe
Received 11 January 2022; Accepted 9 May 2022

Development (2022) 149, dev200527. doi:10.1242/dev.200527

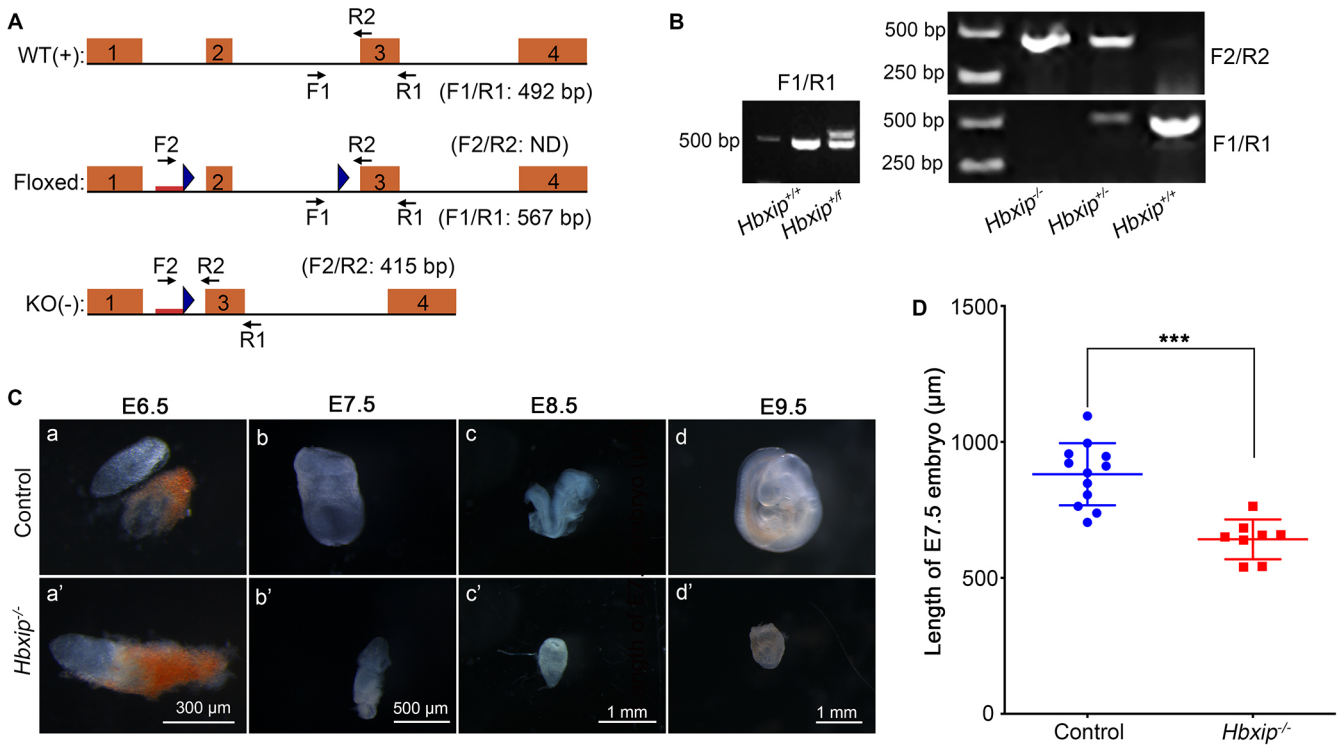

Fig. 1. Embryonic lethality in *Hbxip*$^{-/-}$ mice. (A) Schematic illustration of wild-type (WT), floxed and knockout (KO) alleles of *Hbxip*. Orange rectangles represent *Hbxip* exons, and blue triangles mark loxP sequences. Red bars in the floxed and KO alleles are the exogenous DNA fragment from the targeting vector. Arrows show the primers for genotyping PCR. (B) Representative genotyping PCR results. (C) The morphology of dissected control (including WT and *Hbxip*$^{+/-}$) and *Hbxip*$^{-/-}$ embryos, without any staining, at various stages. (a) E6.5 control, *n*=13; (a′) E6.5 *Hbxip*$^{-/-}$, *n*=4; (b) E7.5 control, *n*=12; (b′) E7.5 *Hbxip*$^{-/-}$, *n*=8; (c) E8.5 control, *n*=8; (c′) E8.5 *Hbxip*$^{-/-}$, *n*=6; (d) E9.5 control, *n*=7; (d′) E9.5 *Hbxip*$^{-/-}$, *n*=4. Scale bars: 300 μm (a,a′), 500 μm (b,b′), 1 mm (c,c′,d,d′). (D) Quantification of the length of E7.5 *Hbxip*$^{-/-}$ and control (including WT and *Hbxip*$^{+/-}$) embryos. Data are shown as mean±s.d. Control, *n*=12; *Hbxip*$^{-/-}$, *n*=8. Statistical analysis was performed with unpaired two-tailed Student's *t*-test. ***P<0.001.

obtained through mating between *Hbxip* floxed mice and *EIIa-cre* mice. *Hbxip*$^{+/-}$ mice are fertile; however, no *Hbxip*$^{-/-}$ mice were born from *Hbxip*$^{+/-}$ intercrosses (Table 1), indicating embryonic lethality of *Hbxip* null mice. To determine the timing of lethality, embryonic day (E)3.5, E6.5, E7.5 and E9.5 embryos from *Hbxip*$^{+/-}$ intercrosses were genotyped, and *Hbxip*$^{-/-}$ embryos were detected at all the analyzed time points (Table 1). However, at 7.5 days postcoitum, *Hbxip*$^{-/-}$ embryos were smaller than wild-type (WT) and *Hbxip*$^{+/-}$ embryos (Fig. 1C,D). At 8.5 and 9.5 days postcoitum, *Hbxip*$^{-/-}$ embryos appeared to be developmentally arrested, compared with their WT and *Hbxip*$^{+/-}$ littermates (Fig. 1C). These data suggest a crucial role of Hbxip in embryonic development.

Table 1. Genotyping of E3.5, E6.5, E7.5 and E9.5 embryos and neonate mice derived from the intercrossing of *Hbxip*$^{+/-}$ mice

	Number of offspring			
Age	+/+	+/–	–/–	Total number
Neonate (***)	57	64	0	121
E9.5	3	4	4‡	11
E7.5	14	18	12‡	44
E6.5	5	8	4	17
E3.5	¶	¶	13§	45

χ^2 test was performed on the number of mouse mutants obtained per stage in comparison to the expected Mendelian ratios. ***P<0.001. ‡Growth was retarded. §Genotypes were determined by the absence of '+' strand. ¶32 *Hbxip*$^{+/+}$ and *Hbxip*$^{+/-}$ embryos were indistinguishable.

Hbxip KO compromises the self-renewal of ESCs

Next, we utilized *in vitro* cultured mouse ESCs to understand the mechanism of Hbxip in embryonic development. *Hbxip* KO ESC lines were constructed using CRISPR/Cas9, with a sgRNA targeting the third exon of *Hbxip* (Fig. 2A). The disruption of *Hbxip* in two independent ESC clones (hereafter referred to as *H*$^{-/-}$*-1* and *H*$^{-/-}$*-2*) with normal karyotype was validated by loss of the *Ban*I site, Sanger sequencing and western blotting (Fig. 2A,B, Fig. S1A-D). Notably, deletion of *Hbxip* compromised the self-renewal of ESCs, demonstrated by reduced proliferation rate and colony-forming capacity (Fig. 2C,D). However, *Hbxip* KO did not change the cell cycle profile or induce apoptosis in ESCs (Fig. S1E, F). The mRNA levels of pluripotency genes, *Nanog*, *Oct4* and *Sox2*, as well as the protein levels of Nanog and Oct4, were decreased in *Hbxip* KO ESCs (Fig. 2B,E). In addition, in undifferentiated ESCs, *Hbxip* KO suppressed the expression of ectodermal, and mesodermal markers, such as nestin, *Celsr2*, *T* and *Dlx3*, whereas the endodermal marker *Gata6* was activated by *Hbxip* KO (Fig. 2F). All these data suggest an essential role of *Hbxip* in ESC self-renewal.

Transcriptomic analysis identified 787 upregulated genes and 1494 downregulated genes shared by *H*$^{-/-}$*-1* and *H*$^{-/-}$*-2* ESCs, compared with WT ESCs (Fig. 2G, Table S2). Gene ontology (GO) annotation revealed that several developmental terms, such as system development, nervous system development and ectoderm development, were enriched in the downregulated genes (Fig. 2H, Fig. S2A). These data imply the involvement of Hbxip in ESC and epiblast differentiation.

Development (2022) 149, dev200527. doi:10.1242/dev.200527

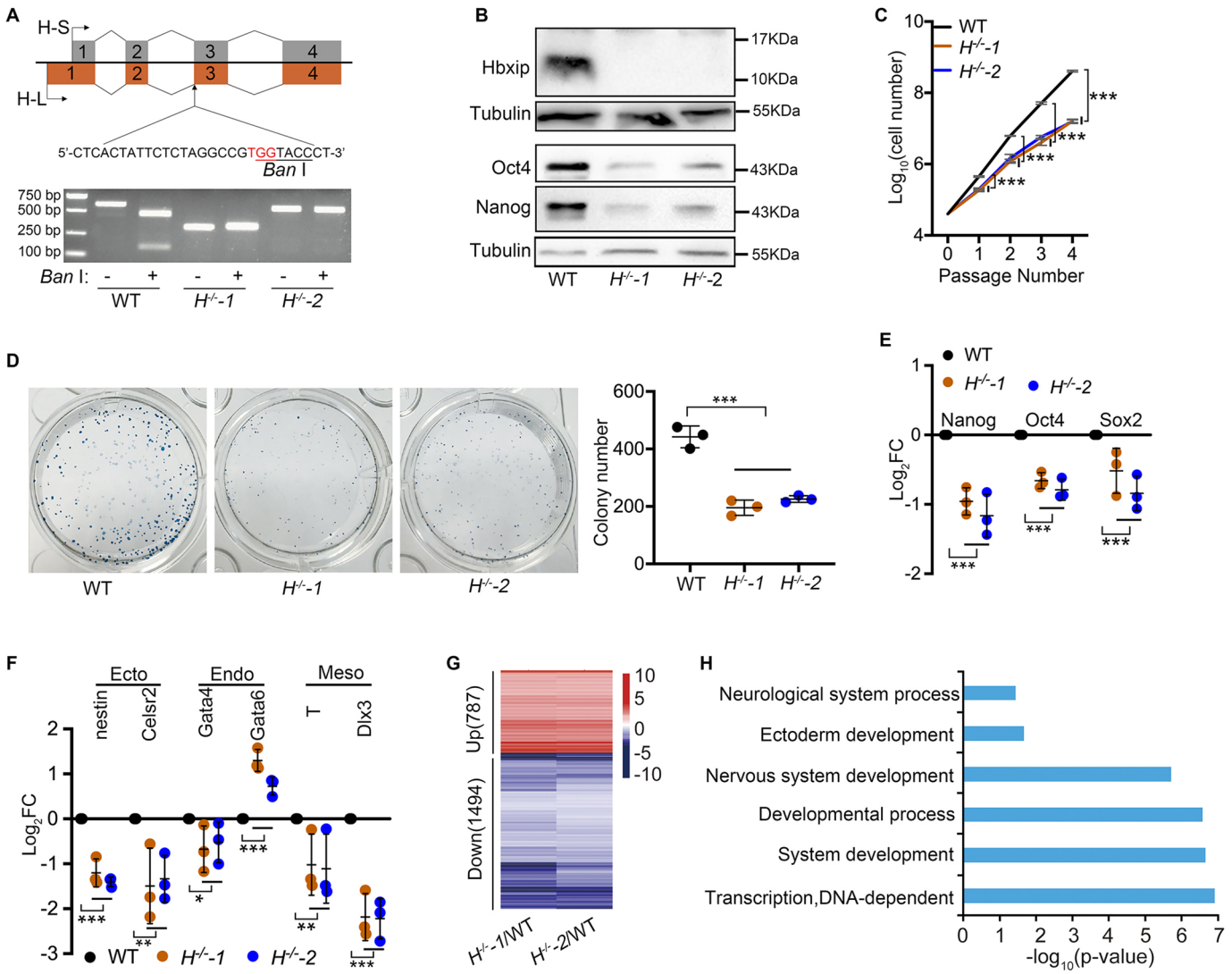

Fig. 2. Compromised self-renewal of *Hbxip*$^{-/-}$ embryonic stem cells (ESCs). (A) Schematic illustration of the strategy for knocking out *Hbxip* in ESCs. The exons of two *Hbxip* isoforms, H-S and H-L, are represented by gray and orange rectangles, respectively. The targeting sequence of sgRNA is shown. The protospacer-adjacent motif (PAM) is highlighted in red, and the *Ban*I site is underlined. The bottom panel shows the validation of *Hbxip* KO in two independent ESC clones by PCR and *Ban*I digestion. (B) Western blots show that the levels of pluripotency factors Nanog and Oct4 are reduced in *Hbxip*$^{-/-}$ ESCs. (C) Growth curves of WT and *Hbxip*$^{-/-}$ ESCs. (D) Colony-forming assay of WT and *Hbxip*$^{-/-}$ ESCs. The left panel shows representative alkaline phosphatase staining images of colony-forming assays. The right panel shows the quantification results of three repeated colony-forming assays. (E) The expression of pluripotency genes *Nanog*, *Oct4* and *Sox2* in WT and *Hbxip*$^{-/-}$ ESCs, measured by quantitative RT-PCR. Fold change (FC) was calculated by comparing with WT ESCs. (F) The expression of differentiation genes in WT and *Hbxip*$^{-/-}$ ESCs. FC was calculated by comparing with WT ESCs. (G) The heatmap showing the differentially expressed genes in *H*$^{-/-}$-1 and *H*$^{-/-}$-2 ESCs, compared with WT ESCs, detected by RNA-seq. (H) Gene ontology (GO) annotation of the downregulated genes in *Hbxip*$^{-/-}$ ESCs. For growth curves, colony formation, quantitative RT-PCR and western blotting, *n*=3. Data are shown as mean±s.d. Statistical analysis was performed with two-way ANOVA. *P<0.05; **P<0.01; ***P<0.001.

Hbxip KO causes differentiation defects in ESCs

We then tested the role of Hbxip in the differentiation of ESCs. Two methods were used to differentiate ESCs, leukemia inhibitory factor (LIF) withdrawal or embryoid body (EB) formation in hanging drops. Under these two differentiation conditions, *Hbxip*$^{-/-}$ ESCs failed to activate differentiation genes, including ectodermal markers, nestin and *Celsr2*, and mesodermal markers, *T* and *Dlx3* (Fig. 3A,B). Through RNA-sequencing (RNA-seq) analysis, we identified 1028 downregulated genes and 482 upregulated genes in differentiated *Hbxip*$^{-/-}$ cells induced by LIF withdrawal, compared with differentiated WT cells (Fig. 3C), and 719 downregulated genes and 655 upregulated genes in day 4 *Hbxip*$^{-/-}$ EBs, compared with WT EBs (Fig. 3D, Table S3). Differentiated *Hbxip*$^{-/-}$ cells by LIF withdrawal and day 4 *Hbxip*$^{-/-}$ EBs shared 481 downregulated genes and 325 upregulated genes (Fig. 3E, Table S3). GO analysis revealed that genes involved in system development, mesoderm development, ectoderm development, embryo development and cell differentiation were enriched in the downregulated genes (Fig. 3F, Fig. S2B).

To further confirm the roles of *Hbxip* in pluripotency maintenance and ESC differentiation, rescue experiments were performed in *H*$^{-/-}$*-1* ESCs by expressing either short-isoform (H-S) or long-isoform (H-L) *Hbxip*. Both H-S and H-L rescued the expression levels of Nanog and Oct4 proteins in undifferentiated ESCs (Fig. 3G, Fig. S2C), as well as the expression of differentiation genes, nestin, *Celsr2*, *T* and *Dlx3*, in differentiated

Development (2022) 149, dev200527. doi:10.1242/dev.200527

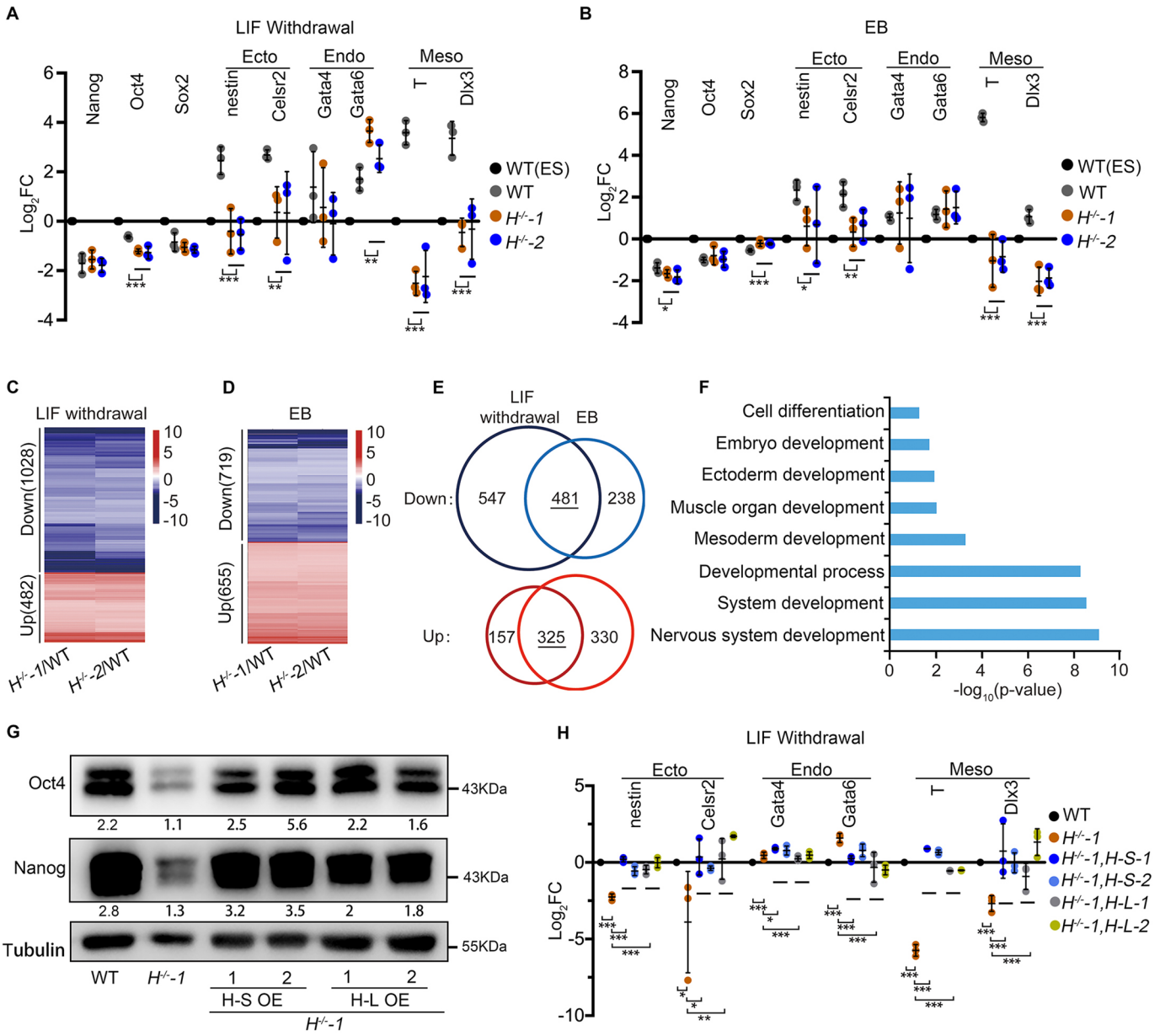

Fig. 3. Differentiation defects of *Hbxip*$^{-/-}$ ESCs. (A,B) The expression of differentiation genes in differentiated WT and *Hbxip*$^{-/-}$ ESCs by leukemia inhibitory factor (LIF) withdrawal for 4 days (A) and in day 4 WT and *Hbxip*$^{-/-}$ embryoid bodies (EBs) (B). FC was calculated by comparing with undifferentiated WT ESCs, marked as WT(ES). (C,D) The heatmaps show the differentially expressed genes in differentiated *Hbxip*$^{-/-}$ ESCs by LIF withdrawal for 4 days (C) and in day 4 *Hbxip*$^{-/-}$ EBs (D), compared with their WT counterparts, detected by RNA-seq. (E) Venn diagrams show the commonly regulated genes (481 downregulated and 325 upregulated genes) by *Hbxip* KO in two differentiation protocols, LIF withdrawal and EB differentiation. (F) GO annotation of the commonly downregulated genes by *Hbxip* KO. (G) Overexpression of *Hbxip*, both H-L and H-S, rescues the expression levels of Nanog and Oct4 proteins in *Hbxip* KO ESCs. The quantified levels of Nanog and Oct4 are shown below the corresponding blots. (H) Overexpression of *Hbxip*, both H-L and H-S, rescues the expression levels of differentiation genes in differentiated *Hbxip* KO ESCs by LIF withdrawal for 4 days. FC was calculated by comparing with differentiated WT ESCs. For quantitative RT-PCR and western blotting, n=3. Data are shown as mean±s.d. Statistical analysis was performed with two-way ANOVA. *P<0.05; **P<0.01; ***P<0.001.

cells (Fig. 3H). These data indicate that Hbxip is required for the proper differentiation of ESCs, particularly toward the ectodermal and mesodermal lineages.

Hbxip$^{-/-}$ embryos are defective in epiblast formation and differentiation

Given the differentiation defects of *Hbxip*$^{-/-}$ ESCs, we tested whether the epiblast properly differentiates into three germ layers, particularly the ectoderm and mesoderm. Immunohistochemical (IHC) analysis with anti-Hbxip antibody allowed us to distinguish *Hbxip*$^{-/-}$ embryos from WT and *Hbxip*$^{+/-}$ embryos (Fig. 4). Hematoxylin and Eosin (H&E) staining showed that the development of the amnion cavity was retarded in E7.5 *Hbxip*$^{-/-}$ embryos (Fig. 4A). Immunofluorescent staining of Oct4 demonstrated that the epiblast in E7.5 *Hbxip*$^{-/-}$ embryos was much smaller than that in E7.5 WT and *Hbxip*$^{+/-}$ embryos, indicating defective epiblast formation (Fig. 4A). At 8.5 days postcoitum, the morphology of WT and *Hbxip*$^{+/-}$ embryos changed drastically with the initiation of somitogenesis. By contrast, the development of *Hbxip*$^{-/-}$ embryos did not progress further.

Development (2022) 149, dev200527. doi:10.1242/dev.200527

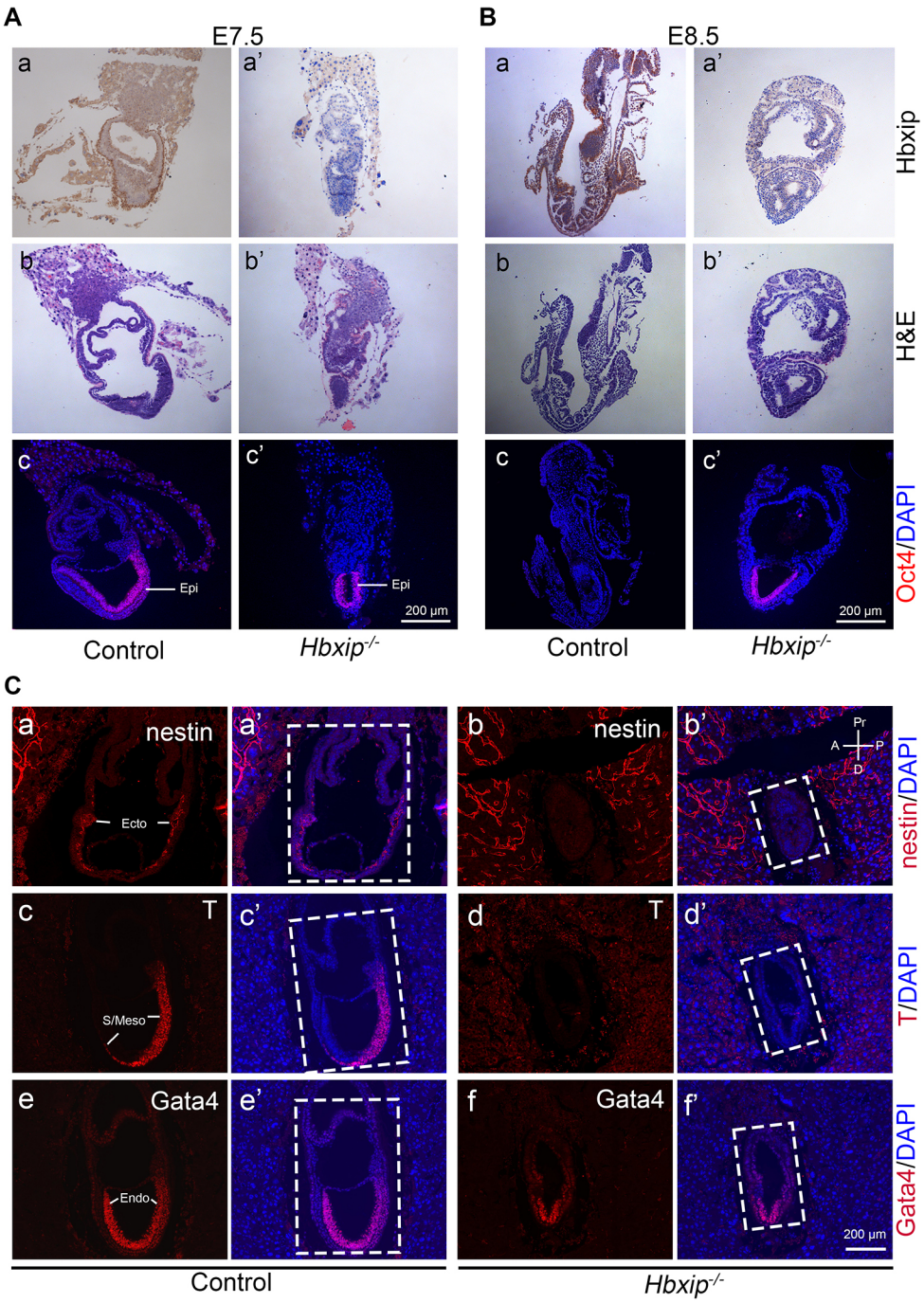

Fig. 4. Defective epiblast proliferation and differentiation in *Hbxip*$^{-/-}$ embryos. (A,B) Control and *Hbxip*$^{-/-}$ E7.5 (A) and E8.5 (B) embryo sections were subjected to immunohistochemical staining for Hbxip (a, a′), H&E staining (b,b′) and immunofluorescence (IF) staining for Oct4 (c,c′). Epi, epiblast. E7.5 (control, *n*=14; *Hbxip*$^{-/-}$, *n*=8); E8.5 (control, *n*=8; *Hbxip*$^{-/-}$, *n*=5). (C) IF staining of control (*n*=7) and *Hbxip*$^{-/-}$ (*n*=3) E7.5 embryo sections for nestin (a,a′,b,b′), T (c,c′,d,d′) and Gata4 (e,e′,f,f′) revealed ectodermal and mesodermal defects in *Hbxip*$^{-/-}$ embryos. Control embryos include WT and *Hbxip*$^{+/-}$ embryos. Dashed line rectangles mark the embryo part. A, anterior; D, distal; Ecto, ectoderm; Endo, endoderm; P, posterior; Pr, proximal; S/Meso, streak/mesoderm. Scale bars: 200 μm.

Importantly, with the formation of three germ layers, Oct4 expression was diminished in E8.5 WT and *Hbxip*$^{+/-}$ embryos, whereas *Hbxip*$^{-/-}$ embryos retained Oct4 expression in the epiblast (Fig. 4B). We further examined the expression of germ layer markers in E7.5 embryos, and found that ectodermal marker nestin and mesodermal marker T were not expressed in E7.5 *Hbxip*$^{-/-}$ embryos, while the expression of endodermal marker Gata4 was not affected by *Hbxip* KO (Fig. 4C). Taken together, these results suggest that *Hbxip*$^{-/-}$ embryo lethality is due to the defects in epiblast proliferation, ectodermal and mesodermal differentiation.

Hbxip is required for the activation of mTORC1

Next, we investigated the molecular mechanism of Hbxip in embryonic development and ESC differentiation. It has been shown that HBXIP functions as a transcriptional cofactor in many cancers (Liu et al., 2012, 2014, 2013; Xu et al., 2014, 2013; Yue et al., 2013; Zhang et al., 2013; Wang et al., 2017a). We first determined the subcellular distribution of Hbxip in ECSs by western blot analysis of cytoplasmic and nuclear fractions of ESCs. The results showed that Hbxip was almost exclusively distributed in the cytoplasm (Fig. 5A), thus excluding its function as a transcriptional cofactor.

To understand the molecular mechanism of Hbxip, co-immunoprecipitation (co-IP) coupled with mass spectrometric analysis was performed to identify Hbxip-interacting proteins. We identified 128 proteins in the H-S and H-L co-IP samples, but not in the control co-IP sample (Fig. 5B, Table S4). GO analysis revealed that these Hbxip-interacting proteins were enriched in mTOR signaling, macroautophagy, PI3K cascade and insulin signaling

Development (2022) 149, dev200527. doi:10.1242/dev.200527

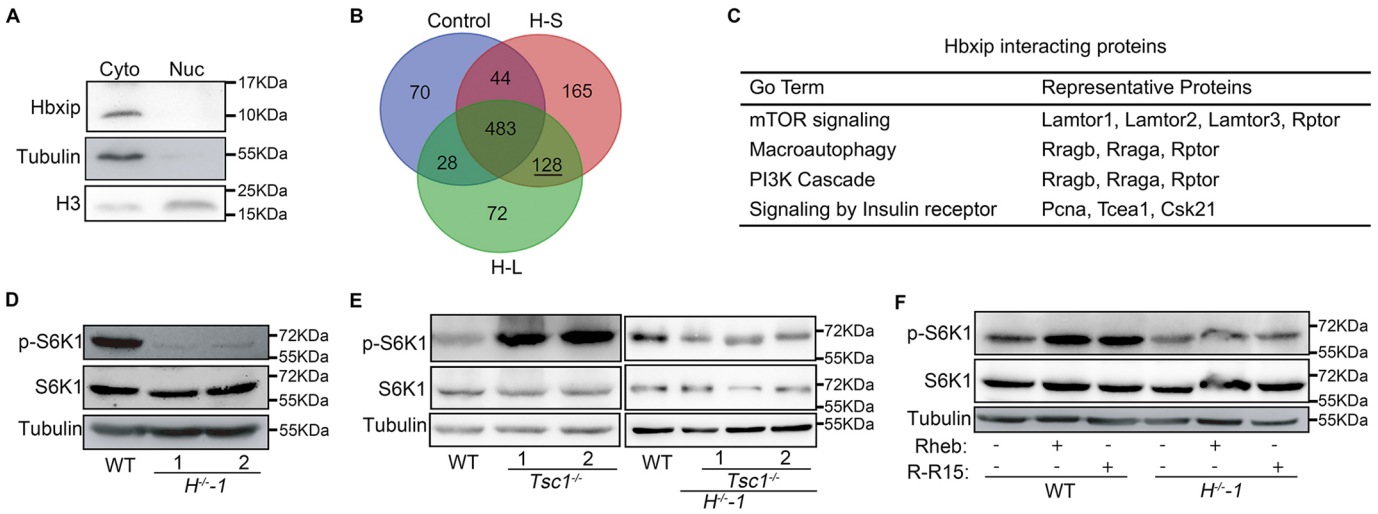

Fig. 5. Hbxip is required for mTORC1 activation. (A) Western blot analysis of Hbxip in the cytoplasmic and nuclear fractions of ESCs. (B) Venn diagram of proteins identified by mass spectrometric analysis. Co-IP experiments were performed with cell extracts from ESCs expressing FLAG-Hbxip (H-L and H-S) and control ESCs with empty vector, using M2 magnetic beads. The resulting immunoprecipitation samples were analyzed by mass spectrometry. 128 proteins identified in both the H-L and H-S samples, but not in the control, are referred to as Hbxip-interacting proteins. (C) GO annotation of the 128 Hbxip-interacting proteins. (D) Western blots of S6K1 and p-S6K1 in WT and *Hbxip*$^{-/-}$ ESCs demonstrate the reduced mTORC1 activity in *Hbxip*$^{-/-}$ ESCs. (E) Western blots of S6K1 and p-S6K1 in WT, *Tsc1*$^{-/-}$, *H*$^{-/-}$-1 and *Tsc1*$^{-/-}$; *H*$^{-/-}$-1 ESCs show that *Tsc1* KO fails to activate mTORC1 in *Hbxip*$^{-/-}$ ESCs. (F) Overexpression of Rheb or Rptor fused with the lysosome-targeting signal of Rheb (R-R15) is unable to activate mTORC1 in *Hbxip*$^{-/-}$ ESCs. WT and *H*$^{-/-}$-1 ESCs were transfected with empty vector, or plasmids expressing Rheb or R-R15. Two days after transfection, ESCs were harvested for western blot analysis. For western blotting, *n*=3.

(Fig. 5C). It has been shown that HBXIP is a member of the Ragulator complex, which recruits mTORC1 to the lysosome, therefore activating the mTORC1 signaling pathway (Bar-Peled et al., 2012). Consistently, three Ragulator components, Lamtor1 (p18), Lamtor2 (p14) and Lamtor3 (MP1), as well as an mTORC1 subunit, Rptor, were identified as Hbxip-interacting proteins (Fig. 5C, Table S4). Thus, we speculated that mTORC1 is the key downstream factor of Hbxip in ESCs and embryos. To test this hypothesis, we first showed that the activity of mTORC1 was reduced in *Hbxip*$^{-/-}$ ESCs and embryos, as indicated by the level of phosphorylated S6K1 and 4EBP1 (Fig. 5D, Fig. S3). Next, we tried to reactivate mTORC1 to rescue the differentiation defects of *Hbxip*$^{-/-}$ ESCs. However, even though knockout of *Tsc1*, or overexpression of Rheb or Rptor fused with the lysosome-targeting signal of Rheb (R-R15) (Sancak et al., 2010; Düvel et al., 2010; Long et al., 2005), successfully activated mTORC1 in WT ESCs, these strategies failed to activate the mTORC1 signaling in *Hbxip*$^{-/-}$ ESCs (Fig. 5E,F, Fig. S4), demonstrating the essential role of Hbxip in mTORC1 activation.

mTORC1 inactivation accounts for the defects in ESC self-renewal and differentiation

Failure in activating mTORC1 in *Hbxip*$^{-/-}$ ESCs indicated that Hbxip is essential for mTORC1 activation. Yet, it rendered the rescue experiment impossible. To prove that inactivation of mTORC1 is responsible for the self-renewal and differentiation defects in *Hbxip*$^{-/-}$ ESCs, an alternative strategy was applied. Instead of the rescue experiment, we knocked out genes encoding other components of the Ragulator complex, such as *Lamtor3* and *Lamtor4*, in ESCs (Fig. S5). Similar to *Hbxip*$^{-/-}$ ESCs, *Lamtor3*$^{-/-}$ and *Lamtor4*$^{-/-}$ ESCs displayed self-renewal defects, including reduced protein levels of Oct4 and Nanog, downregulated *Oct4*, *Nanog*, and *Sox2* mRNA expression, slower proliferation rate and decreased colony forming capacity (Fig. 6A-D). Moreover, upon differentiation, *Lamtor3*$^{-/-}$ and *Lamtor4*$^{-/-}$ ESCs also failed to activate ectodermal and mesodermal markers (Fig. 6E,F), just as we observed in *Hbxip*$^{-/-}$ ESCs (Fig. 3A,B). All these data indicate that inactivation of mTORC1 leads to the self-renewal and differentiation defects in ESCs.

DISCUSSION

In this study, we demonstrated that Hbxip is essential for embryonic development and ESC differentiation. *Hbxip*$^{-/-}$ ESCs, as well as *Lamtor3*$^{-/-}$ and *Lamtor4*$^{-/-}$ ESCs, with disrupted Ragulator complex, displayed differentiation defects toward ectodermal and mesodermal lineages (Fig. 3A,B, Fig. 6E,F). Moreover, *Hbxip*$^{-/-}$, *p14*$^{-/-}$ and *p18*$^{-/-}$ mice, lacking subunits of the Ragulator complex, are embryonic lethal, and retarded growth of these embryos was detected at the same developmental stage, around E7-E8 (Fig. 1C, Table 1) (Nada et al., 2009; Teis et al., 2006). These data indicate that the phenotypes of *Hbxip*$^{-/-}$ embryos and ESCs are mainly caused by loss of function of the Ragulator complex, rather than lack of the transcriptional co-activator role of Hbxip.

The Ragulator complex is required for the activation of mTORC1 by amino acids (Sancak et al., 2010; Bar-Peled et al., 2012). Consistently, the mTORC1 activity was reduced in *Hbxip*$^{-/-}$ ESCs (Fig. 5D, Fig. S3A). KO of *Tsc1* and overexpression of Rheb or R-R15 failed to activate mTORC1 in the absence of Hbxip (Fig. 5E,F). In addition, the reduced mTORC1 activity by disruption of the Ragulator complex allowed us to investigate the function of mTORC1 in post-implantation embryo development. Deletion of mTORC1 components, mTor and Rptor, results in peri-implantation embryonic death around E5.5-E6.5 (Gangloff et al., 2004; Murakami et al., 2004; Guertin et al., 2006), thus preventing studying the role of mTORC1 in later stage of embryogenesis. Nevertheless, *Hbxip*$^{-/-}$, *p14*$^{-/-}$ and *p18*$^{-/-}$ embryos, in which mTORC1 activity is presumably attenuated, developed further after implantation, and retarded growth appeared around E7-E8. The reduced size of E7.5 *Hbxip*$^{-/-}$ embryos might be attributed to slower cell proliferation rate caused by decreased mTORC1 activity. Moreover, the differentiation defects of *Hbxip*$^{-/-}$ ESCs (Fig. 3A,B) imply that the *Hbxip*$^{-/-}$ epiblast might be defective in

Development (2022) 149, dev200527. doi:10.1242/dev.200527

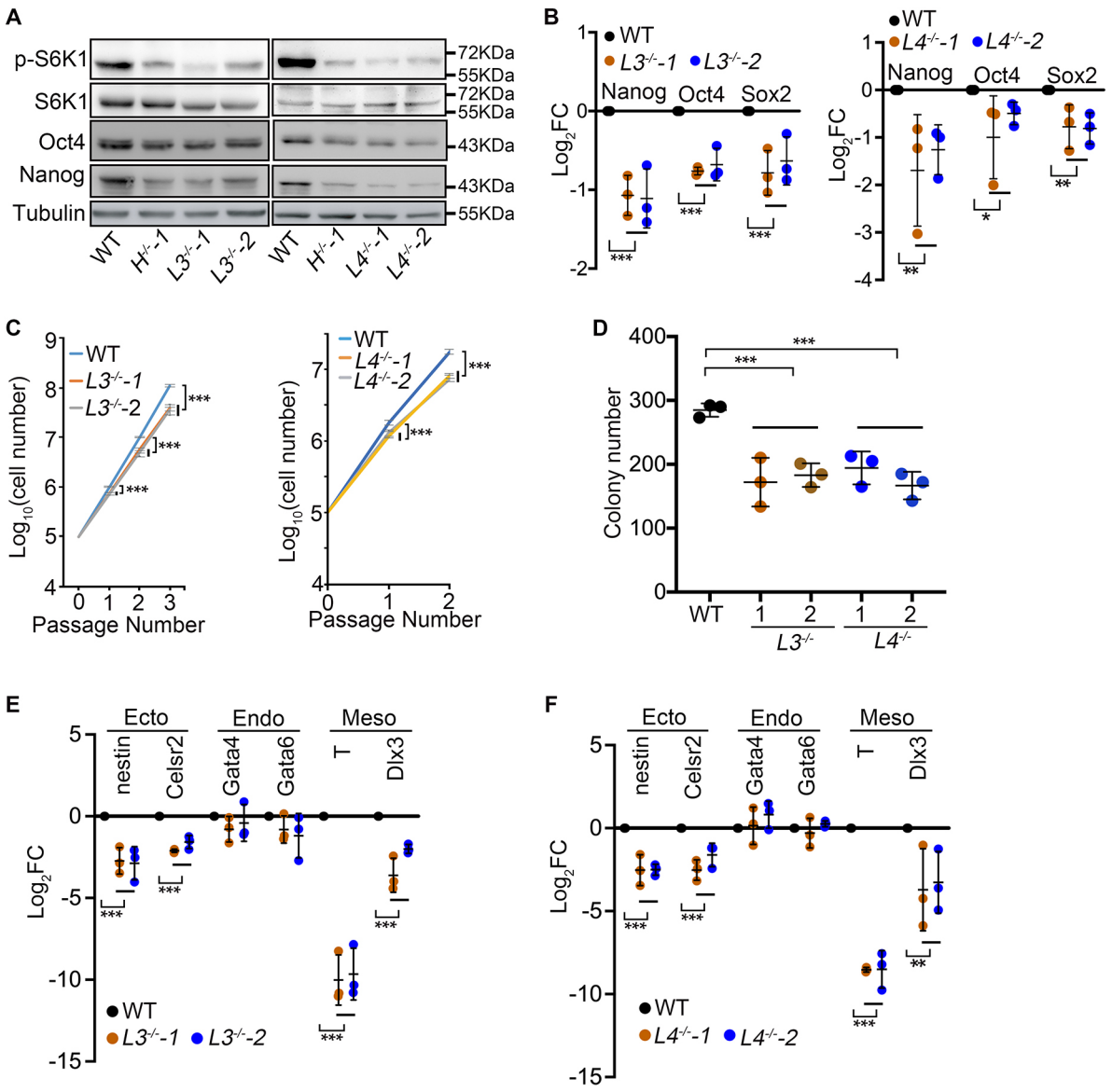

Fig. 6. Differentiation defects in ESCs lacking other Ragulator subunits. (A) Western blots of S6K1, p-S6K1, Nanog and Oct4 in WT, *Hbxip*$^{-/-}$, *Lamtor3*$^{-/-}$ (*L3*$^{-/-}$) and *Lamtor4*$^{-/-}$ (*L4*$^{-/-}$) ESCs. (B) The expression levels of pluripotency genes in WT, *L3*$^{-/-}$ and *L4*$^{-/-}$ ESCs measured by quantitative RT-PCR. FC was calculated by comparing with WT ESCs. (C) Growth curves of WT, *L3*$^{-/-}$ and *L4*$^{-/-}$ ESCs. (D) Colony-forming assays of WT, *L3*$^{-/-}$ and *L4*$^{-/-}$ ESCs. (E,F) The expression levels of differentiation genes in differentiated WT, *L3*$^{-/-}$ (E) and *L4*$^{-/-}$ (F) ESCs. ESCs were differentiated for 96 h in the absence of LIF. The resulting differentiated cells were harvested for quantitative RT-PCR. FC was calculated by comparing with differentiated WT ESCs. For growth curves, colony formation, quantitative RT-PCR and western blotting, *n*=3. Data are shown as mean±s.d. Statistical analysis was performed with two-way ANOVA. **P*<0.05; ***P*<0.01; ****P*<0.001.

differentiation. Indeed, the differentiation of the *Hbxip*$^{-/-}$ epiblast was compromised, as indicated by the sustained expression of Oct4 in E8.5 *Hbxip*$^{-/-}$ embryos, and the failure in expressing ectodermal marker nestin and mesodermal marker T in in E7.5 *Hbxip*$^{-/-}$ embryos (Fig. 4), suggesting that mTORC1 activity is pivotal for epiblast differentiation. Consistent with this, inhibition of mTOR by INK128 induces a paused pluripotent state in the blastocyst, mimicking diapause (Bulut-Karslioglu et al., 2016), further supporting the role of mTORC1 in the exit from pluripotency.

Even though *Hbxip*$^{-/-}$ epiblasts and *Hbxip*$^{-/-}$ ESCs were both defective in activating the expression of ectodermal and mesodermal markers, Oct4 expression was sustained in E8.5 *Hbxip*$^{-/-}$ embryos, while the downregulation of *Oct4* was not affected during the differentiation of *Hbxip*$^{-/-}$ ESCs, most likely due to *in vitro* differentiation of ESCs being unable to recapture all the features of *in vivo* embryo development, even though it mimics the *in vivo* development of embryos. It is possible that the downregulation of Oct4 in developing embryos might require the activation of differentiation genes, whereas the repression of *Oct4* could be triggered by LIF withdrawal during ESC differentiation, regardless of whether differentiation genes are activated or not. Another seemingly conflicting point is that differentiation genes were not activated in *Hbxip*$^{-/-}$ ESCs, in which pluripotency genes were downregulated. This is likely due to the unique effect of mTOR inhibition in ESCs. mTOR inhibition induces pausing of ESCs, which display global transcriptional suppression, including both pluripotency genes and differentiation genes (Bulut-Karslioglu et al., 2016). Thus, the reduced mTORC1 activity in *Hbxip*$^{-/-}$ ESCs

Development (2022) 149, dev200527. doi:10.1242/dev.200527

may be responsible for simultaneous downregulation of pluripotency genes and differentiation genes.

mTOR signaling is involved in growth and disease through regulating gene transcription, mRNA degradation, protein synthesis, autophagy, and lipid and carbohydrate metabolism (Giguère, 2018; Villa et al., 2021; Cho et al., 2021; Mossmann et al., 2018; Saxton and Sabatini, 2017). Further studies are required to elucidate how mTORC1 regulated by the Ragulator complex promotes the differentiation of the epiblast and ESCs. *Hbxip*$^{-/-}$, *Lamtor3*$^{-/-}$ and *Lamtor4*$^{-/-}$ ESCs provide an excellent *in vitro* experimental system for mechanistic investigation.

MATERIALS AND METHODS

Mice

Nankai Animal Care and Use Committee approved the use of mice for this research (approval number: 2021-SYDWLL-000469). The care and use of experimental animals complied with relevant institutional and national animal welfare laws, guidelines and policies. *EIIa-cre* mice (Lakso et al., 1996), which express Cre at a very early stage of pre-implantation embryogenesis, most likely at the zygote stage, and are useful for whole-body and germ line deletion of floxed allele, were purchased from Shanghai Model Organisms. *Hbxip*$^{-/-}$ mice were obtained by crossing *Hbxip*$^{+/-}$ mice. All mice were maintained in the C57BL/6 background. Genotyping was performed as described previously (Qin et al., 2019). DNA was isolated from dissected embryos or the tail tips of 2-week-old mice, and then analyzed by PCR. The sequences of primers (illustrated in Fig. 1A) were as follows: F1, 5′-TTTTTGTCACTCTCGCCTTTG-3′; R1, 5′-GCTGGTATGTACTCACCCATT-3′; F2, 5′-GCTCTATGGCTTCTGAG-GCGGAA-3′; R2, 5′-CTCATCCGACAGGGTACCACGG-3′.

Embryo collection

Embryo manipulation experiments were carried out as described previously (Zhou et al., 2018). Female *Hbxip*$^{+/-}$ mice (4-6 weeks) were induced to superovulate by intraperitoneal injection of 5 IU pregnant mare serum gonadotropin (Calbiochem) and, 48 h later, 5 IU human chorionic gonadotropin (hCG; Sigma-Aldrich). Then, females were mated with male *Hbxip*$^{+/-}$ mice overnight. The next morning, females were checked for the presence of a vaginal plug, designated as E0.5. Zygote and E3.5 embryos were flushed from oviducts at day 0.5 or day 3.5 post-hCG. E6.5, E7.5, E8.5 and E9.5 embryos were collected at corresponding time points after successful mating.

Histological analysis

Embryos were dissected from mice immediately after euthanasia, fixed in 4% paraformaldehyde for up to 24 h, stored in 70% ethanol and embedded in paraffin. Then, 5 µm-thick sections were prepared using a rotary microtome (Leica) and mounted on glass slides. After deparaffinization, sections were stained with H&E for histological analysis.

IHC analysis

After deparaffinization, sections were boiled in 1× citrate buffer (ORIGENE, ZLI-9064) and then microwaved at low power for 15 min. After cooling to room temperature (RT), the sections were blocked with 5% bovine serum albumin at RT for 45 min, and then incubated with primary antibody (anti-Hbxip, Cell Signaling Technology, 14633S, 1:200) at RT for 1 h. After three washes with 1×PBS buffer and 3% H_2O_2 treatment for 10 min, the slides were incubated with goat anti-rabbit IgG conjugated to horseradish peroxidase (HRP) (ORIGENE, ZB-2301) at RT for 1 h. HRP activity was detected by a Vectastain ABC (avidin-biotin-peroxidase) kit (Vector Laboratories), as recommended by the manufacturer. The slides were examined using a Leica Microscope, and images were captured with a Leica DFC420C camera.

Immunofluorescence (IF) analysis

IF analysis of paraffin sections was carried out as described previously (Qin et al., 2019). After deparaffinization, the sections were blocked with 5% goat serum at RT for 45 min, then incubated with primary antibody [anti-Oct4, Abcam, ab181557, 1:200; anti-nestin, Absin, abs137231, 1:100; anti-Brachyury (T), Abmart, T58977, 1:100; anti-Gata4, Abcam, ab84593, 1:200; anti-p-S6K1, Sigma-Aldrich, SAB4301518, 1:100] at RT for 1 h. After washing three times in 1×PBS buffer, the slides were incubated with Alexa Fluor 594-conjugated goat anti-rabbit IgG (Invitrogen, A11037) at RT for 1 h. The nuclei were stained with 4′,6-diamidino-2-phenylindol (DAPI; Thermo Fisher Scientific). All images were captured with a Leica DM3000 microscope with DFC420C camera.

Cell culture and transfection

Mouse ESCs (E14 and its derivatives) were cultured in high-glucose Dulbecco's modified Eagle medium (GIBCO) supplemented with 15% fetal bovine serum (Hyclone), 1% penicillin/streptomycin, 1% L-glutamine, 1% β-mercaptoethanol (Sigma-Aldrich), 1% non-essential amino acids (Invitrogen) and 1000 U/ml LIF (ESGRO, Chemicon), plated on gelatin-coated tissue culture dishes and grown in humidified 5% CO_2 at 37°C. Transfection was carried out with Lipofectamine® 3000 (Invitrogen) according to the manufacturer's instructions. For construction of stably transfected clones, puromycin (1.25 µM) selection was applied for 5-7 days, starting from 24 h after transfection. All ESC lines were routinely tested for mycoplasma contamination.

Vector construction

pX330-U6-Chimeric_BB-CBh-hSpCas9 (pX330) vector (Addgene plasmid #42230) was used to construct gene knockout plasmids targeting *Hbxip*, *Tsc1*, *Lamtor3* and *Lamtor4*. sgRNA was designed in Zhang Feng's online website (http://crispr.mit.edu/). A pair of sgRNA oligonucleotides containing the guide sequence were annealed and ligated to the *Bbs*I-linearized vector pX330. The sgRNA oligonucleotides targeting *Hbxip* were 5′-CACC-GTCTCACTATTCTCTAGGCCG-3′ and 5′-AAACCGGCCTAGAGAAT-AGTGAGAC-3′. The sgRNA oligonucleotides targeting *Tsc1* were 5′-CACCGGTGGTCAGGATGTGCAATAC-3′ and 5′-AAACGTATTGCA-CATCCTGACCACC-3′. The sgRNA oligonucleotides targeting *Lamtor3* were 5′-CACCGTCCTGTACAAAAAGTTGCCA-3′ and 5′-AAACTGGC-AACTTTTTGTACAGGAC-3′. The sgRNA oligonucleotides targeting *Lamtor4* were 5′-CACCGTGTGCTGACCAACTCCGAGA-3′ and 5′-AAA-CTCTCGGAGTTGGTCAGCACAC-3′; 5′-CACCGCTGCTTGCTCATCG-TTCTCA-3′ and 5′-AAACTGAGAACGATGAGCAAGCAGC-3′.

Cell proliferation assay

ESCs (1×10^5) were plated in 12-well plates in triplicates. Cells were passaged continuously and counted every 2 days.

Western blotting

ESCs were collected and dissociated in cold lysis buffer (20 mM HEPES, pH 7.7; 5 mM KCl; 1.5 mM $MgCl_2$; 2 mM DTT; 2 mM PMSF) for 30 min on ice. Then, the cell lysate was centrifuged at 12,000 ***g***, for 15 min at 4°C. Protein concentration was measured using a BCA Protein Assay Kit (Beyotime). The samples were resolved with SDS-PAGE gel and transferred onto PVDF membrane. Then, the PVDF membrane was incubated in blocking buffer for 1 h at RT, followed by incubating with primary antibodies (anti-Hbxip, Cell Signaling Technology, 14633S, 1:2000; anti-Nanog, Bethyl Laboratories, A300-397A, 1:2000; anti-Oct4, Santa Cruz Biotechnology, sc-5279, 1:1000; anti-tubulin, Sigma-Aldrich, ASB4800087, 1:2000; anti-S6K1, Sigma-Aldrich, SAB4502686, 1:1000; anti-p-S6K1, Sigma-Aldrich, SAB4301518, 1:1000; anti-H3, Abcam, ab1791, 1:2000; anti-Tsc1, Absin, abs131176, 1:2000; anti-MP1/Lamtor3, Novus, NBP1-50631, 1:2000; anti-C7orf59/Lamtor4, Cell Signaling Technology, D4P6O, 1:2000; anti-p-4EBP1, Cell Signaling Technology, 2855, 1:2000; anti-4EBP1, Cell Signaling Technology, 9452, 1:2000) at 4°C overnight. After washing three times, the membrane was incubated with HRP-conjugated secondary antibodies at RT for 1 h. Immunoreactivity was detected by ECL Plus (Beyotime). Digital images were taken with an automatic chemiluminescence imaging analysis system (Tanon).

Co-IP

ESC extracts were prepared using lysis buffer (20 mM Tris-HCl, pH 8; 137 mM NaCl; 10% glycerol; 1% NP-40; 2 mM EDTA, supplemented with

protease inhibitor and PMSF). FLAG antibody (M2)-conjugated magnetic beads were washed in TBS buffer (50 mM Tris-HCl, 150 mM NaCl, pH 7.4) three times. ESC extracts were incubated with 15 µl M2 beads at 4°C overnight. The immunoprecipitates were washed three times using TBS buffer, eluted in 2× SDS-PAGE loading buffer and subjected to mass spectrometric analysis.

RNA purification and quantitative reverse-transcription PCR (RT-PCR)

Total RNA was purified using TRIZOL (Ambion) according to the manufacturer's instructions. cDNA was synthesized using a Reverse Transcription Kit (Roche). PCR reactions were performed with FastStart Universal SYBR Green Master (Roche) in a Bio-Rad IQ5 system. PCR cycling conditions were 95°C for 2 min, 40 cycles of 95°C for 15 s, 58°C for 15 s and 72°C for 30 s, and then a melting curve of the amplified DNA was acquired. Quantification of target genes was normalized with β-actin. Primers are listed in Table S1.

RNA-seq

Total RNA was purified using an RNeasy Mini Kit (Qiagen) according to the manufacturer's instructions. Construction of an RNA-seq library, sequencing with BGISEQ-500 and bioinformatic analysis were performed by BGI Tech (Shenzhen, China).

Alkaline phosphatase (AP) assay

After washing once with PBS, mouse ESCs were stained with AP Substrate Kit III (Vector Laboratories), according to the manufacturer's instructions.

Colony-forming assay

Mouse ESCs were suspended in ESC medium and cultured in a six-well plate (800 cells per well). After 4-6 days of culture, ESCs were stained for AP. The AP-positive colonies were counted under a microscope.

EB-forming assay

Mouse ESCs were suspended in LIF-free ESC medium (40,000 cells/ml) and cultured in 25 µl hanging drops. EBs were collected on day 4.

Cell cycle analysis

Cells were collected and fixed with 70% ethanol, then stained with staining buffer (5 µg/ml propidium iodide, 1 mg/ml RNase A) for 30 min at 37°C and analyzed by FACSCalibur flow cytometer (BD Biosciences). Modfit software was used to analyze the results.

Apoptosis analysis

Apoptosis was detected by an Annexin V-EGFP Apoptosis Detection Kit (Beyotime, C1067S) as recommended by the manufacturer. Cells were harvested and washed in 1× PBS once. Then they were resuspended in 195 µl Annexin V- EGFP binding buffer supplemented with 5 µl Annexin V-EGFP and 10 µl propidium iodide, incubated at RT for 20 min and analyzed by a FACSCalibur flow cytometer (BD Biosciences). Flow Jo software was used to analyze the results.

Karyotype analysis

Cells were incubated with 0.3 µg/ml nocodazole for 3-5 h to enrich cells at metaphase. These metaphase-enriched cells were harvested and exposed to 0.075 M KCl solution at 37°C for 25 min, then fixed with cold methanol: glacial acetic acid (3:1) buffer at least four times and spread onto clean slides. Finally, the cells were stained with DAPI. Cells with more than 39 chromosomes were counted.

Data processing and statistical analysis

All images were processed with Photoshop 2021 (Adobe) and ImageJ (National Institutes of Health). All data were analyzed using Excel (Microsoft) and Prism (GraphPad Software). All experiments were confirmed with at least three independent experiments, and at least three control or mutant embryos (the exact sample size is shown in figure legends) were used for immunostaining. Statistical analyses were performed with χ^2 test, unpaired two-tailed Student's *t*-test or two-way ANOVA, as indicated in the figure legends. The quantitative results were presented as the mean±s.d. $P<0.05$ was considered statistically significant.

Acknowledgements

We thank the core facility at College of Life Sciences, Nankai University.

Competing interests

The authors declare no competing or financial interests.

Author contributions

Conceptualization: L.Y., L.C.; Formal analysis: Y.Q., P.N.; Investigation: Y.Q., P.N., Q.Z., X.W., X.D., Z.Y., L.W.; Resources: L.Y.; Writing - original draft: Y.Q., P.N., L.C.; Writing - review & editing: L.Y., L.C.; Supervision: L.C.; Project administration: L.C.; Funding acquisition: L.C.

Funding

L.C. was supported by the National Key Research and Development Program of China (2021YFA1101002 and 2018YFA0107002), the National Natural Science Foundation of China (31871485), the Natural Science Foundation of Tianjin City (18JCJQJC48400), the 111 Project Grant (B08011) and the Fundamental Research Funds for the Central Universities. Y.Q. was supported by the China Postdoctoral Science Foundation (2019M660980) and the National Natural Science Foundation of China (32000600).

Data availability

RNA-seq data are available at Gene Expression Omnibus (accession number GSE104242).

Peer review history

The peer review history is available online at https://journals.biologists.com/dev/article-lookup/doi/10.1242/dev.200527.

References

Bar-Peled, L., Schweitzer, L. D., Zoncu, R. and Sabatini, D. M. (2012). Ragulator is a GEF for the rag GTPases that signal amino acid levels to mTORC1. *Cell* **150**, 1196-1208. doi:10.1016/j.cell.2012.07.032

Bulut-Karslioglu, A., Biechele, S., Jin, H., Macrae, T. A., Hejna, M., Gertsenstein, M., Song, J. S. and Ramalho-Santos, M. (2016). Inhibition of mTOR induces a paused pluripotent state. *Nature* **540**, 119-123. doi:10.1038/nature20578

Cheng, D., Liang, B. and Li, Y. (2014). HBXIP expression predicts patient prognosis in breast cancer. *Med. Oncol.* **31**, 210. doi:10.1007/s12032-014-0210-6

Cho, S., Lee, G., Pickering, B. F., Jang, C., Park, J. H., He, L., Mathur, L., Kim, S.-S., Jung, S., Tang, H.-W. et al. (2021). mTORC1 promotes cell growth via m(6)A-dependent mRNA degradation. *Mol. Cell* **81**, 2064-2075.e68. doi:10.1016/j.molcel.2021.03.010

Düvel, K., Yecies, J. L., Menon, S., Raman, P., Lipovsky, A. I., Souza, A. L., Triantafellow, E., Ma, Q., Gorski, R., Cleaver, S. et al. (2010). Activation of a metabolic gene regulatory network downstream of mTOR complex 1. *Mol. Cell* **39**, 171-183. doi:10.1016/j.molcel.2010.06.022

Fujii, R., Zhu, C., Wen, Y., Marusawa, H., Bailly-Maitre, B., Matsuzawa, S.-I., Zhang, H., Kim, Y., Bennett, C. F., Jiang, W. et al. (2006). HBXIP, cellular target of hepatitis B virus oncoprotein, is a regulator of centrosome dynamics and cytokinesis. *Cancer Res* **66**, 9099-9107. doi:10.1158/0008-5472.CAN-06-1886

Gangloff, Y.-G., Mueller, M., Dann, S. G., Svoboda, P., Sticker, M., Spetz, J.-F., Um, S. H., Brown, E. J., Cereghini, S., Thomas, G. et al. (2004). Disruption of the mouse mTOR gene leads to early postimplantation lethality and prohibits embryonic stem cell development. *Mol. Cell. Biol.* **24**, 9508-9516. doi:10.1128/MCB.24.21.9508-9516.2004

Giguère, V. (2018). Canonical signaling and nuclear activity of mTOR-a teamwork effort to regulate metabolism and cell growth. *FEBS J.* **285**, 1572-1588. doi:10.1111/febs.14384

Guertin, D. A., Stevens, D. M., Thoreen, C. C., Burds, A. A., Kalaany, N. Y., Moffat, J., Brown, M., Fitzgerald, K. J. and Sabatini, D. M. (2006). Ablation in mice of the mTORC components raptor, rictor, or mLST8 reveals that mTORC2 is required for signaling to Akt-FOXO and PKCα, but not S6K1. *Dev. Cell* **11**, 859-871. doi:10.1016/j.devcel.2006.10.007

Hu, N., Zhang, J., Cui, W., Kong, G., Zhang, S., Yue, L., Bai, X., Zhang, Z., Zhang, W., Zhang, X. et al. (2011). miR-520b regulates migration of breast cancer cells by targeting hepatitis B X-interacting protein and interleukin-8. *J. Biol. Chem.* **286**, 13714-13722. doi:10.1074/jbc.M110.204131

Lakso, M., Pichel, J. G., Gorman, J. R., Sauer, B., Okamoto, Y., Lee, E., Alt, F. W. and Westphal, H. (1996). Efficient in vivo manipulation of mouse genomic

sequences at the zygote stage. *Proc. Natl. Acad. Sci. USA* **93**, 5860-5865. doi:10.1073/pnas.93.12.5860

Li, X. and Liu, S. (2016). Suppression of HBXIP reduces cell proliferation, migration and invasion in vitro, and tumorigenesis in vivo in human urothelial carcinoma of the bladder. *Cancer Biother. Radiopharm.* **31**, 311-316. doi:10.1089/cbr.2016.2038

Li, N., Wang, Y., Che, S., Yang, Y., Piao, J., Liu, S. and Lin, Z. (2017). HBXIP over expression as an independent biomarker for cervical cancer. *Exp. Mol. Pathol.* **102**, 133-137. doi:10.1016/j.yexmp.2017.01.009

Li, H., Wang, Z., Li, Y., Fang, R., Wang, H., Shi, H., Zhang, X., Zhang, W. and Ye, L. (2018). Hepatitis B X-interacting protein promotes the formation of the insulin gene-transcribing protein complex Pdx-1/Neurod1 in animal pancreatic β-cells. *J. Biol. Chem.* **293**, 2053-2065. doi:10.1074/jbc.M117.809582

Liu, S., Li, L., Zhang, Y., Zhang, Y., Zhao, Y., You, X., Lin, Z., Zhang, X. and Ye, L. (2012). The oncoprotein HBXIP uses two pathways to up-regulate S100A4 in promotion of growth and migration of breast cancer cells. *J. Biol. Chem.* **287**, 30228-30239. doi:10.1074/jbc.M112.343947

Liu, Q., Bai, X., Li, H., Zhang, Y., Zhao, Y., Zhang, X. and Ye, L. (2013). The oncoprotein HBXIP upregulates Lin28B via activating TF II D to promote proliferation of breast cancer cells. *Int. J. Cancer* **133**, 1310-1322. doi:10.1002/ijc.28154

Liu, F., You, X., Wang, Y., Liu, Q., Liu, Y., Zhang, S., Chen, L., Zhang, X. and Ye, L. (2014). The oncoprotein HBXIP enhances angiogenesis and growth of breast cancer through modulating FGF8 and VEGF. *Carcinogenesis* **35**, 1144-1153. doi:10.1093/carcin/bgu021

Liu, B., Wang, T., Wang, H., Zhang, L., Xu, F., Fang, R., Li, L., Cai, X., Wu, Y., Zhang, W. et al. (2018). Oncoprotein HBXIP enhances HOXB13 acetylation and co-activates HOXB13 to confer tamoxifen resistance in breast cancer. *J. Hematol. Oncol.* **11**, 26. doi:10.1186/s13045-018-0577-5

Long, X., Lin, Y., Ortiz-Vega, S., Yonezawa, K. and Avruch, J. (2005). Rheb binds and regulates the mTOR kinase. *Curr. Biol.* **15**, 702-713. doi:10.1016/j.cub.2005.02.053

Marusawa, H., Matsuzawa, S., Welsh, K., Zou, H., Armstrong, R., Tamm, I. and Reed, J. C. (2003). HBXIP functions as a cofactor of survivin in apoptosis suppression. *EMBO J.* **22**, 2729-2740. doi:10.1093/emboj/cdg263

Melegari, M., Scaglioni, P. P. and Wands, J. R. (1998). Cloning and characterization of a novel hepatitis B virus x binding protein that inhibits viral replication. *J. Virol.* **72**, 1737-1743. doi:10.1128/JVI.72.3.1737-1743.1998

Mossmann, D., Park, S. and Hall, M. N. (2018). mTOR signalling and cellular metabolism are mutual determinants in cancer. *Nat. Rev. Cancer* **18**, 744-757. doi:10.1038/s41568-018-0074-8

Murakami, M., Ichisaka, T., Maeda, M., Oshiro, N., Hara, K., Edenhofer, F., Kiyama, H., Yonezawa, K. and Yamanaka, S. (2004). mTOR is essential for growth and proliferation in early mouse embryos and embryonic stem cells. *Mol. Cell Biol.* **24**, 6710-6718. doi:10.1128/MCB.24.15.6710-6718.2004

Nada, S., Hondo, A., Kasai, A., Koike, M., Saito, K., Uchiyama, Y. and Okada, M. (2009). The novel lipid raft adaptor p18 controls endosome dynamics by anchoring the MEK-ERK pathway to late endosomes. *EMBO J.* **28**, 477-489. doi:10.1038/emboj.2008.308

Qin, Y., Zhou, Y., Shen, Z., Xu, B., Chen, M., Li, Y., Chen, M., Behrens, A., Zhou, J., Qi, X. et al. (2019). WDR62 is involved in spindle assembly by interacting with CEP170 in spermatogenesis. *Development* **146**, dev174128. doi:10.1242/dev.174128

Sancak, Y., Bar-Peled, L., Zoncu, R., Markhard, A. L., Nada, S. and Sabatini, D. M. (2010). Ragulator-Rag complex targets mTORC1 to the lysosomal surface and is necessary for its activation by amino acids. *Cell* **141**, 290-303. doi:10.1016/j.cell.2010.02.024

Saxton, R. A. and Sabatini, D. M. (2017). mTOR signaling in growth, metabolism, and disease. *Cell* **168**, 960-976. doi:10.1016/j.cell.2017.02.004

Shi, H., Fang, R., Li, Y., Li, L., Zhang, W., Wang, H., Chen, F., Zhang, S., Zhang, X. and Ye, L. (2016). The oncoprotein HBXIP suppresses gluconeogenesis through modulating PCK1 to enhance the growth of hepatoma cells. *Cancer Lett.* **382**, 147-156. doi:10.1016/j.canlet.2016.08.025

Teis, D., Taub, N., Kurzbauer, R., Hilber, D., De Araujo, M. E., Erlacher, M., Offterdinger, M., Villunger, A., Geley, S., Bohn, G. et al. (2006). p14-MP1-MEK1 signaling regulates endosomal traffic and cellular proliferation during tissue homeostasis. *J. Cell Biol.* **175**, 861-868. doi:10.1083/jcb.200607025

Villa, E., Sahu, U., O'hara, B. P., Ali, E. S., Helmin, K. A., Asara, J. M., Gao, P., Singer, B. D. and Ben-Sahra, I. (2021). mTORC1 stimulates cell growth through SAM synthesis and m(6)A mRNA-dependent control of protein synthesis. *Mol. Cell* **81**, 2076-2093.e79. doi:10.1016/j.molcel.2021.03.009

Wang, Y., Fang, R., Cui, M., Zhang, W., Bai, X., Wang, H., Liu, B., Zhang, X. and Ye, L. (2017a). The oncoprotein HBXIP up-regulates YAP through activation of transcription factor c-Myb to promote growth of liver cancer. *Cancer Lett.* **385**, 234-242. doi:10.1016/j.canlet.2016.10.018

Wang, Y., Li, N., Che, S., Jin, T., Piao, J., Liu, S. and Lin, Z. (2017b). HBXIP suppression reduces cell proliferation and migration and its overexpression predicts poor prognosis in non-small-cell lung cancer. *Tumour Biol.* **39**, 1010428317709675. doi:10.1177/1010428317709675

Wang, Y., Sun, J., Li, N., Che, S., Jin, T., Liu, S. and Lin, Z. (2017c). HBXIP overexpression is correlated with the clinical features and survival outcome of ovarian cancer. *J. Ovarian Res.* **10**, 26. doi:10.1186/s13048-017-0322-7

Wen, Y., Golubkov, V. S., Strongin, A. Y., Jiang, W. and Reed, J. C. (2008). Interaction of hepatitis B viral oncoprotein with cellular target HBXIP dysregulates centrosome dynamics and mitotic spindle formation. *J. Biol. Chem.* **283**, 2793-2803. doi:10.1074/jbc.M708419200

Wu, Y., Wang, X., Xu, F., Zhang, L., Wang, T., Fu, X., Jin, T., Zhang, W. and Ye, L. (2020). The regulation of acetylation and stability of HMGA2 via the HBXIP-activated Akt-PCAF pathway in promotion of esophageal squamous cell carcinoma growth. *Nucleic Acids Res.* **48**, 4858-4876. doi:10.1093/nar/gkaa232

Xu, F., You, X., Liu, F., Shen, X., Yao, Y., Ye, L. and Zhang, X. (2013). The oncoprotein HBXIP up-regulates Skp2 via activating transcription factor E2F1 to promote proliferation of breast cancer cells. *Cancer Lett.* **333**, 124-132. doi:10.1016/j.canlet.2013.01.029

Xu, F., Zhu, X., Han, T., You, X., Liu, F., Ye, L., Zhang, X., Wang, X. and Yao, Y. (2014). The oncoprotein hepatitis B X-interacting protein promotes the migration of ovarian cancer cells through the upregulation of S-phase kinase-associated protein 2 by Sp1. *Int. J. Oncol.* **45**, 255-263. doi:10.3892/ijo.2014.2411

Yue, L., Li, L., Liu, F., Hu, N., Zhang, W., Bai, X., Li, Y., Zhang, Y., Fu, L., Zhang, X. et al. (2013). The oncoprotein HBXIP activates transcriptional coregulatory protein LMO4 via Sp1 to promote proliferation of breast cancer cells. *Carcinogenesis* **34**, 927-935. doi:10.1093/carcin/bgs399

Zhang, Y., Zhao, Y., Li, L., Shen, Y., Cai, X., Zhang, X. and Ye, L. (2013). The oncoprotein HBXIP upregulates PDGFB via activating transcription factor Sp1 to promote the proliferation of breast cancer cells. *Biochem. Biophys. Res. Commun.* **434**, 305-310. doi:10.1016/j.bbrc.2013.02.123

Zhang, W., Lu, Z., Kong, G., Gao, Y., Wang, T., Wang, Q., Cai, N., Wang, H., Liu, F., Ye, L. et al. (2014). Hepatitis B virus X protein accelerates hepatocarcinogenesis with partner survivin through modulating miR-520b and HBXIP. *Mol. Cancer* **13**, 128. doi:10.1186/1476-4598-13-128

Zhou, Y., Qin, Y., Qin, Y., Xu, B., Guo, T., Ke, H., Chen, M., Zhang, L., Han, F., Li, Y. et al. (2018). Wdr62 is involved in female meiotic initiation via activating JNK signaling and associated with POI in humans. *PLoS Genet.* **14**, e1007463. doi:10.1371/journal.pgen.1007463

Zhou, X., Wang, X., Duan, J., Sun, W., Chen, Z., Li, Q., Ou, Z., Jiang, G., Ren, X. and Liu, S. (2019a). HBXIP protein overexpression predicts the poor prognosis of pancreatic ductal adenocarcinomas. *Pathol. Res. Pract.* **215**, 343-346. doi:10.1016/j.prp.2018.12.016

Zhou, X.-L., Zhu, C.-Y., Wu, Z.-G., Guo, X. and Zou, W. (2019b). The oncoprotein HBXIP competitively binds KEAP1 to activate NRF2 and enhance breast cancer cell growth and metastasis. *Oncogene* **38**, 4028-4046. doi:10.1038/s41388-019-0698-5

Zou, W., Ma, X., Yang, H., Hua, W., Chen, B. and Cai, G. (2017). Hepatitis B X-interacting protein promotes cisplatin resistance and regulates CD147 via Sp1 in ovarian cancer. *Exp. Biol. Med.* **242**, 497-504. doi:10.1177/1535370216685007

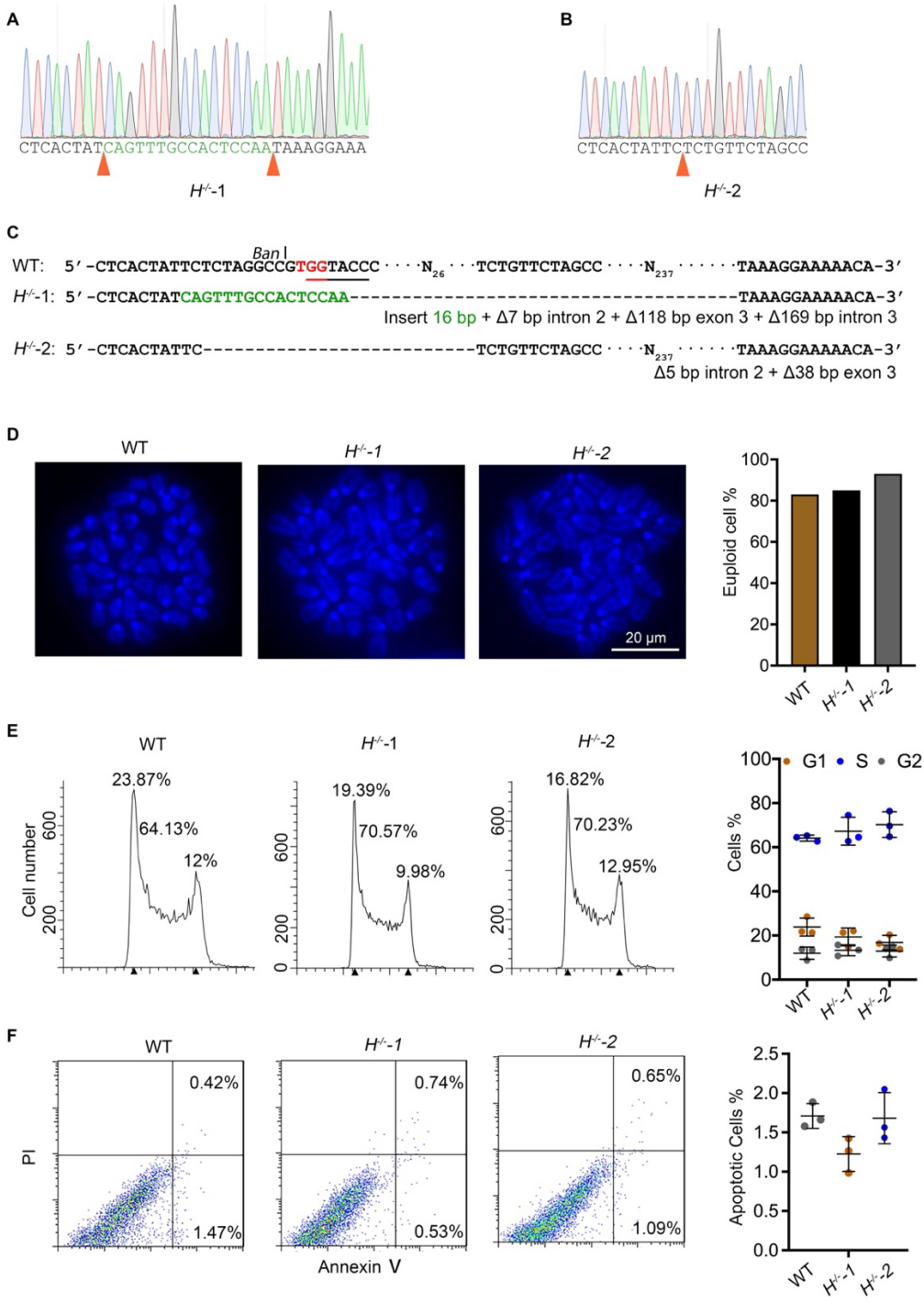

Fig. S1. Related to Fig. 2. Validation of *Hbxip*$^{-/-}$ ESC clones.

(A) and (B) Sequencing chromatograph of the *Hbxip* gene around the Cas9 targeting site in *H*$^{-/-}$-1 (A) and *H*$^{-/-}$-2 (B) ESCs. Orange triangles mark the indel mutations introduced by Cas9 cutting. (C) Sequence alignment of the *Hbxip* gene around the Cas9 targeting site in WT, *H*$^{-/-}$-1 and *H*$^{-/-}$-2 ESCs. (D-F) Karyotyping (D), cell cycle (E), and apoptosis (F) analyses of WT and *Hbxip*$^{-/-}$ ESCs. (D) More than 30 metaphase spreads were counted for each cell line. Scale bar: 20 μm. (E) and (F) For cell cycle and apoptosis analyses, data are shown as mean ± SD (n=3). Statistical analysis was performed with two-way ANOVA test. $p > 0.05$ was considered as statistical non-significance.

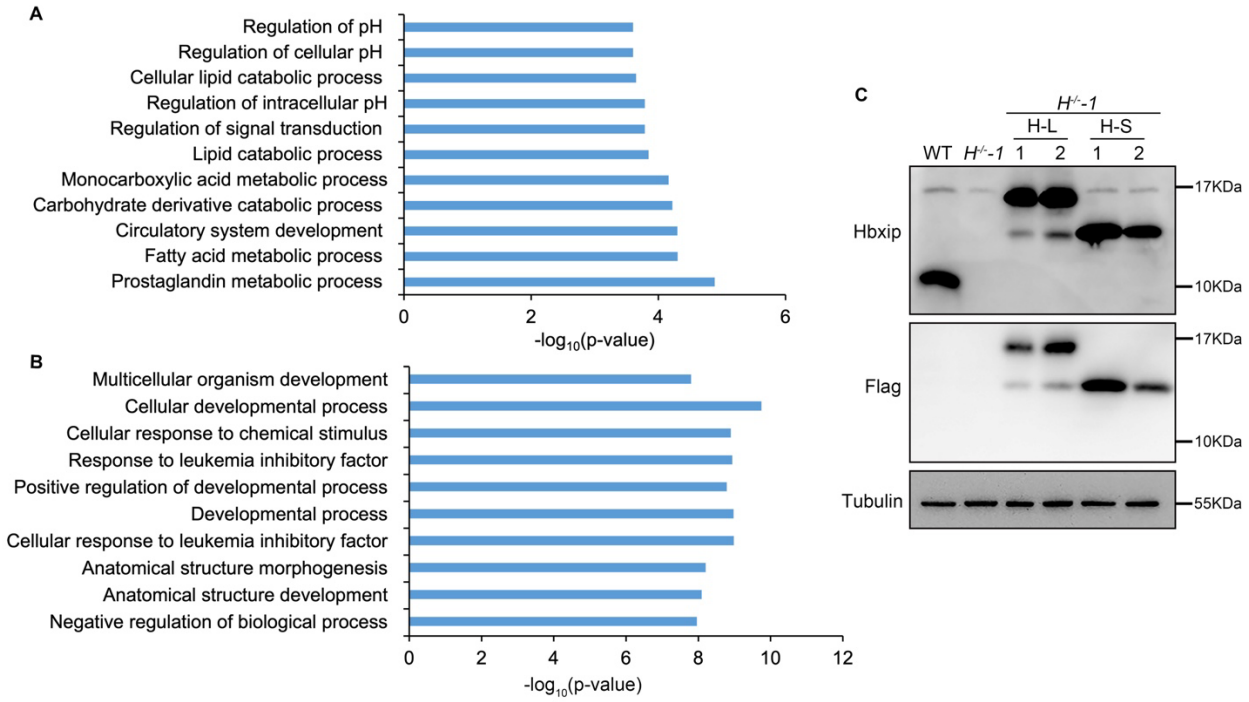

Fig. S2. Related to Figs 2, 3. *Hbxip KO* affects gene expression and mTORC1 activity.
(A) GO annotation of the upregulated genes in *Hbxip*$^{-/-}$ ESCs (Related to Fig. 2G, H). (B) GO annotation of the commonly upregulated genes by *Hbxip* KO (Related to Fig. 3C-F). (C) Validation of the overexpression of Flag tagged Hbxip, including H-L and H-S (Related to Fig. 3G).

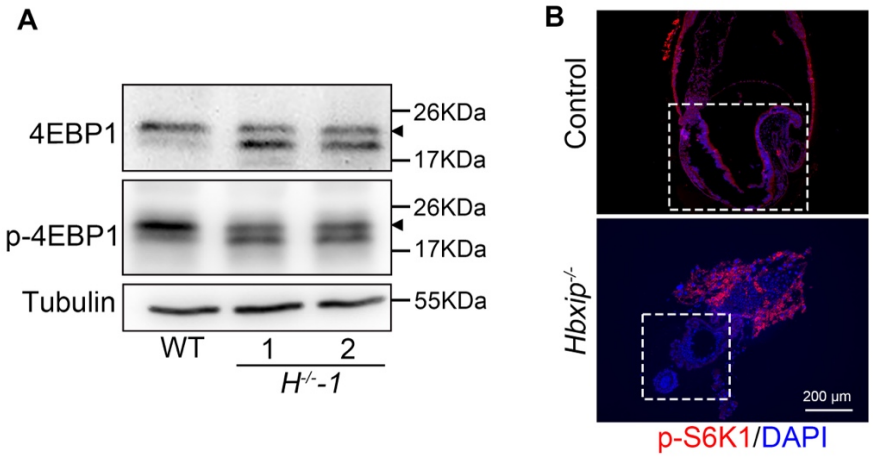

Fig. S3. Related to Fig. 5. Reduced mTOCRC1 activity in *Hbxip*$^{-/-}$ ESCs and embryos.
(A) Western blots of 4EBP1 and p-4EBP1 in WT and *Hbxip*$^{-/-}$ ESCs demonstrate the reduced mTORC1 activity in *Hbxip*$^{-/-}$ ESCs. Triangles mark the specific bands for 4EBP1 and p-4EBP1. (B) Immunofluorescence staining of p-S6K1 in control and *Hbxip*$^{-/-}$ E8.5 embryo sections. Dashed rectangles mark the embryo part. Control (including WT and *Hbxip*$^{+/-}$), n=4; *Hbxip*$^{-/-}$, n=4. Scale bar: 200 μm.

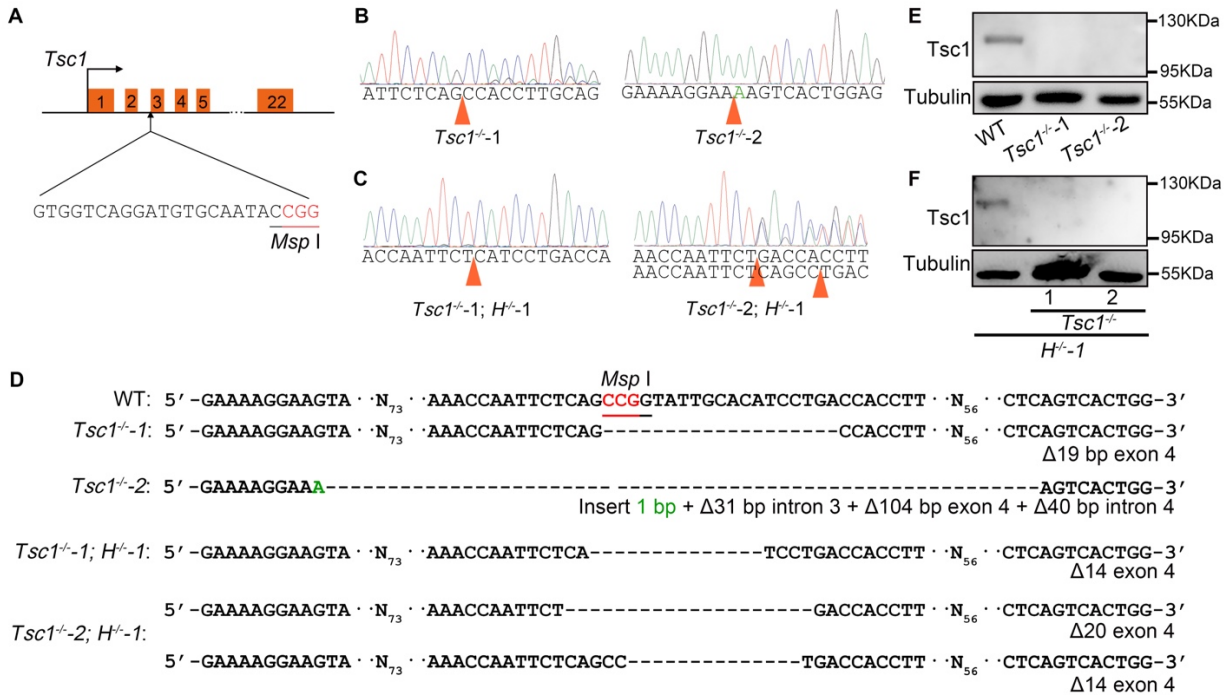

Fig. S4. Related to Fig. 5. Validation of *Tsc1*$^{-/-}$ ESC clones.

(A) Schematic illustration of the strategy for knocking out *Tsc1* in ESCs. The targeting sequence of sgRNA is shown. The protospacer-adjacent motif (PAM) is highlighted in red, and the *Msp* I site is underlined. (B) and (C) Sequencing chromatograph of the *Tsc1* gene around the Cas9 targeting site in *Tsc1*$^{-/-}$ (B) and *Tsc1*$^{-/-}$; *H*$^{-/-}$-1 (C) ESCs. Orange triangles mark the indel mutations introduced by Cas9 cutting. (D) Sequence alignment of the *Tsc1* gene around the Cas9 targeting site in WT, *Tsc1*$^{-/-}$ and *Tsc1*$^{-/-}$; *H*$^{-/-}$-1 ESCs. (E) and (F) Validation of Tsc1 knockout in *Tsc1*$^{-/-}$ (E) and *Tsc1*$^{-/-}$; *H*$^{-/-}$-1 (F) ESCs by Western blot.

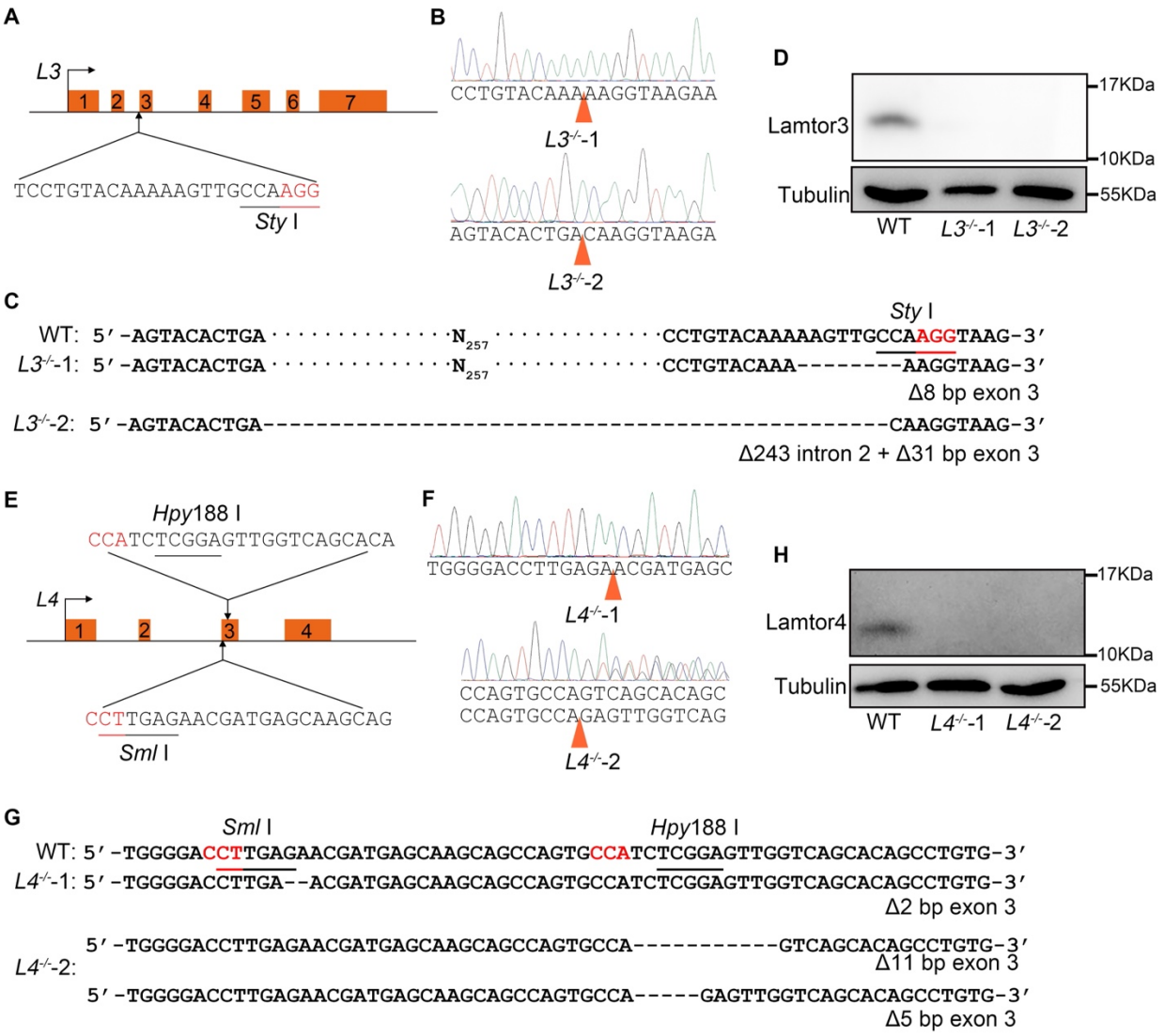

Fig. S5. Related to Fig. 6. Validation of *Lamtor3*$^{-/-}$ and *Lamtor4*$^{-/-}$ ESC clones.

(A) and (E) Schematic illustration of the strategy for knocking out *Lamtor3* (A) and *Lamtor4* (E) in ESCs. The targeting sequences of sgRNAs (one for *Lamtor3* and two for *Lamtor4*) are shown. The protospacer-adjacent motif (PAM) is highlighted in red, and the *Sty* I, *Sml* I and *Spy*188 I sites are underlined. (B) and (F) Sequencing chromatograph of the *Lamtor3* and *Lamtor4* gene around the Cas9 targeting site in *Lamtor3*$^{-/-}$ (B) and *Lamtor4*$^{-/-}$ (F) ESC clones. Orange triangles mark the indel mutations introduced by Cas9 cutting. (C) and (G) Sequence alignment of the *Lamtor3* (C) and *Lamtor4* (G) gene around the Cas9 targeting site in WT, *Lamtor3*$^{-/-}$ (C) and *Lamtor4*$^{-/-}$ (G) ESCs. (D) and (H) Validation of Lamtor3 (D) and Lamtor4 (H) knockout in *Lamtor3*$^{-/-}$ (D) and *Lamtor4*$^{-/-}$ (H) ESCs by Western blot.

Table S1. Primers for quantitative RT-PCR

Gene	Forward	Reverse
Nanog	TACAAGGGTCTGCTACTGAGATGC	TTGGGACTGGTAGAAGAATCAGGG
Oct4	ATCAGCTTGGGCTAGAGAAGGATG	AAAGGTGTCCCTGTAGCCTCATAC
Sox2	GCGGAGTGGAAACTTTTGTCC	CGGGAAGCGTGTACTTATCCTT
Nestin	CTGGATCTGGAAGTCAACAGAGGT	ATCCTCAGTTTCCACTCCTGTAGC
Gata4	GCTATGCATCTCCTGTCACTCAGA	CCAAGTCCGAGCAGGAATTTGAAG
Gata6	CTTCTCCTTCTACACAAGCGACCA	ATACTTGAGGTCACTGTTCTCGGG
T	CATCGGAACAGCTCTCCAACCTAT	TACCATTGCTCACAGACCAGAGAC
Celsr2	CACGATGGCCTGAGGGTTT	CCTTGTGGAGAAAGGTGTCCT
Dlx3	CACTGACCTGGGCTATTACAGC	GAGATTGAACTGGTGGTGGTAG
β-Actin	CAGAAGGAGATTACTGCTCTGGCT	TACTCCTGCTTGCTGATCCACATC

Table S2. Differentially expressed genes (DEGs) identified in *Hbxip*$^{-/-}$ ESCs, compared to WT ESCs.

Click here to download Table S2

Table S3. DEGs identified in differentiated *Hbxip*$^{-/-}$ ESCs, compared to differentiated WT ESCs.

WT, *H*$^{-/-}$-1, and *H*$^{-/-}$-2 ESCs were differentiated for 4 days by two methods, LIF withdrawal and EB. RNA purified from these differentiated cells were subjected to RNA-seq analysis.

Click here to download Table S3

Table S4. Hbxip interacting proteins identified by co-IP and mass spectrometry.

Click here to download Table S4